

Monocrystalline free standing 3D yttrium iron garnet magnon nano resonators

F. Heyroth,¹ C. Hauser,² P. Trempler,² P. Geyer,² F. Syrowatka,¹
R. Dreyer,² S.G. Ebbinghaus,³ G. Woltersdorf,² and G. Schmidt^{2,1,*}

¹*Interdisziplinäres Zentrum für Materialwissenschaften,*

Martin-Luther-Universität Halle-Wittenberg, D-06120 Halle, Germany

²*Institut für Physik, Martin-Luther-Universität Halle-Wittenberg, D-06120 Halle, Germany*

³*Institut für Chemie, Martin Luther Universität Halle-Wittenberg, D-06120 Halle, Germany*

Nano electromechanical systems are hot candidates for coupling of electromagnetic fields to mechanical oscillations in quantum information processing¹⁻⁵. Yttrium Iron Garnet (YIG) would be an extremely interesting material for nanoresonators with high quality factors as it exhibits extremely long lifetimes for spin waves⁶ (magnons) and as a single crystalline garnet material also has low losses for mechanical waves (phonons). As magneto-elastic coupling provides a suitable link between both excitations^{7,8} 3D YIG nanoresonators would allow to create a new class of high-Q magnetomechanical nano-oscillators. However, up to now no method was available to shape three dimensional nanostructures from monocrystalline YIG. Here we show that using electron beam lithography and room temperature pulsed laser deposition free standing YIG nanobridges and cantilevers can be fabricated. After annealing the bridges crystallize and follow the GGG substrate lattice which acts as a locally defined and controlled nucleation site, resulting in a monocrystalline bridge with low Gilbert damping. These results may allow to downscale magnon-based coupling of qubits and mechanical resonators well into the sub-micrometer regime.

PACS numbers:

I. INTRODUCTION

Yttrium iron garnet is the material with the lowest known Gilbert damping⁶ making it ideal for spin wave based applications, often referred to as magnonics⁹. Nanopatterning of thin films with reasonable quality has been demonstrated¹⁰⁻¹⁴ and a number of examples for magnon based devices have already been published¹⁵⁻¹⁸. Besides the perspective of developing magnonics as a post CMOS technology for complex data processing also the use of magnons for quantum computing has gained interest in recent years and the coupling of a magnon mode in a YIG sphere to a single qubit has already been demonstrated in 2015¹⁹. On the other hand over the past decade a concept was put forward where micromechanical resonators capacitively coupled to electric fields are used for quantum computing². For example in so called transmons mechanical resonator modes with high quality factor are coupled to electromagnetic modes in a superconducting qubit^{20,21}. In this respect the potential of YIG goes even beyond the above mentioned magnonics because it also allows for the coupling of magnons to mechanical oscillations or phonons. In relatively large YIG spheres in the sub-mm range the coupling of magnons to phonons has already been demonstrated⁸. Nevertheless, the investigation of this coupling in nanostructures still remains elusive, basically due to a lack of suitable YIG nanoresonators. While 2D patterning of YIG can meanwhile be considered state of the art, the fabrication of 3D nanostructures seemed unfeasible due to the necessary patterning steps. It would, however, be extremely attractive to work for example with micron- or sub-micron sized YIG bridges or cantilevers, as the mechanical resonance frequencies of this kind of device may

be easily engineered to fall in the range of typical magnon frequencies²².

II. PATTERNING ISSUES

Fabrication processes for 3D nanostructures can be divided in two different categories, namely additive and subtractive patterning processes. In an additive process the material is deposited in the desired shape, which, on the nanoscale can usually be obtained by lithography, evaporation, and lift-off. A typical example is the fabrication of metallic air bridges and 3D structures by electron beam lithography and lift-off, which is well known since more than a decade²³⁻²⁵. The process is often used to form electrical contacts to nano-devices. A major drawback of the process, however, is the necessity of low temperature deposition of the material of the bridge because of the limited temperature stability of electron beam resists. This limitation mostly prevents its use for the patterning of monocrystalline materials, which usually need to be deposited at high temperatures. In principle, inorganic solid state resists might solve this problem, however, crystalline growth, also known as epitaxy, usually requires a suitable crystalline substrate. The absence of the necessary crystalline surface underneath the span of a bridge results in polycrystalline material growth at least in these areas. As a consequence, monocrystalline cantilevers, for example from III/V-semiconductors are fabricated by subtractive processes²⁶. A semiconductor multilayer is first patterned laterally into the shape of the cantilever by lithography and etching. Subsequently a sacrificial layer underneath the cantilever is removed resulting in a free standing structure. The possible shapes

which can be achieved by this process are limited because the structure is cut from a flat layer. For typical YIG-substrate combinations this process does not work because no suitable sacrificial layers are known. In the past years a new kind of deposition method for thin film YIG has been demonstrated in which amorphous YIG films are first deposited at room temperature on gallium gadolinium garnet (GGG) using either pulsed laser deposition^{27,28} or sputtering²⁹. In a subsequent annealing step the material adapts the lattice structure of the substrate resulting in thin single-crystalline YIG films. Surprisingly the quality of these films in terms of damping surpasses the quality of thin films deposited at high temperature²⁷⁻²⁹.

This deposition method is compatible to organic resists and standard optical or electron beam lithography and the fabrication of laterally nanopatterned YIG with reasonably small Gilbert damping constants has been demonstrated recently^{10,11,13}. Only the fabrication of 3D nanostructures has not yet been achieved although the use of those structures for quantum information processing as described above could be enormous. Even if the fabrication of bridges by lift-off can be done when the material is deposited at room temperature, it appears questionable whether the recrystallisation throughout a bridge can be achieved. While in a thin film crystallization needs to progress only vertically from the substrate to the film surface (with a typical distance of 100 nm or less) in a bridge the crystallization starts at the base of the supporting pillars which are in contact with the substrate and then needs to progress around bends and through the entire span of the bridge in order to achieve a monocrystalline structure. Any additional nucleation site for crystallization may disturb the process and introduce an additional grain boundary. As we show in the following it is not only possible to use a 3D lift-off process for YIG but also the crystallization which indeed starts at the substrate can extend throughout the complete bridge structure even over distances in excess of one micrometer. Defects are only generated where large strain is induced during the growth process or where crystallization fronts emanating from two separate contact points to the substrate meet in the middle of a bridge.

III. FABRICATION

Figs. 1a-d schematically show the applied process flow. A thick PMMA layer on a GGG substrate is patterned using electron beam lithography at different acceleration voltages for the span (low voltage and pillars (high voltage) of the bridges, respectively (Fig. 1a). Details are given in the methods section. The resulting structure after development is shown in Fig. 1b. It exhibits holes down to the substrate for the pillars and a groove for the span of the bridge. At the sides the groove has a slight undercut which later facilitates the lift-off process. Onto the developed structure the YIG is deposited by

PLD at room temperature (Fig. 1c). Subsequent lift-off and resist removal results in a bridge structure (Fig. 1d) which is finally annealed. Fig. 1e shows a scanning electron microscopy (SEM) image of bridges of various lengths after lift-off prior to annealing. For the experiment shown here the pillars are not placed at the end of the bridges. This design yields an overhang at the end to combine the investigation of short cantilevers fixed on one end only with that of bridges which are fixed on both ends. Bridges and cantilevers are flat after the lift-off process of material deposited at room temperature which is expected to be strain-free. After annealing (Fig. 1f) the bridge itself remains mostly unchanged, however, the overhang is bent upward indicating the presence of strain, which is created during the annealing process leading to elastic deformation. Most likely a similar strain also exists in the bridge, however, the mechanical restriction by the second pillar prevents a comparable deformation.

IV. STRUCTURAL CHARACTERIZATION

While the SEM pictures show that the molding of the material is successful, the local crystalline quality can only be assessed by transmission electron microscopy (TEM). Atomic resolution TEM has been performed on different bridges after annealing (details described in the methods section). Fig. 2a shows a cross sectional view of a small bridge with a span of approx. 850 nm and a height between span and substrate of 75 nm. As it turns out, the following different areas of the structure yield all relevant information: The pillars, the transition between pillar and span, the center of the span and two points on the span left and right of the center. In the pillars the material has no visual defects in the volume and the crystalline orientation corresponds exactly to the substrate lattice. This behavior has already been observed in large area structures deposited on GGG²⁷. In the transition region from the pillar to the span, where the layer thickness is thinner, some defects are present in the crystal, most likely due to increased strain. The span volume is again quasi defect free. Only in the center a single defect can be identified (Fig. 2b). The origin of the defect becomes obvious when the lattice of the span left and right of the defect is analyzed. From pillar to center the lattice appears flawless and the orientation seems similar to that of the pillars. For a precise comparison of the orientations we make three Fourier transforms of the lattice on the left and on the right hand side of the defect and exactly at the center (Fig. 2d). Using false colors red, green, and blue we superimpose the three Fourier transforms and we find that there is a very small rotation of the lattice axes between left, center, and right. The tilt angle is approx. 1.5° . For better visibility Fig. 2c shows an example for a bridge with a more pronounced lattice rotation of almost 3° . A comparison shows that on the left hand side of the defect the lattice is rotated clockwise while on the right hand side it is rotated counter-clockwise with respect to

the center of the bridge and also to the substrate. Apparently the strain at the transition from the pillar did not prevent the lattice from maintaining its structure but has led to some elastic relaxation during the crystallization process which has slightly tilted the lattice in the span. As this process starts simultaneously at both pillars two crystallization fronts of lattices tilted with respect to each other meet at the center of the span, resulting in a mismatch that can only be compensated for by the formation of a crystalline defect.

Since the strain depends on the geometry of the bridge we have investigated bridges with an increased height (150 nm under the span, Fig. 2e) or a longer span (2.8 μm , Fig. 2f). For the increased height the transition from pillar to span is far less perfect than for the previously discussed sample. TEM images show a strongly increased number of defects in this area. Nevertheless, apart from a very small tilt (0.5°) the lattice orientation in the span corresponds to that of substrate and pillar. Still the lattice rotation increases again towards the center of the span where the deviation between left and right side again reaches 1.5°. The center of the bridge now shows more than a single defect but a clear boundary where the crystallization fronts have met during the annealing. Careful alignment in TEM even reveals a different contrast on both sides of this boundary, indicating that in addition to the observed tilt the two parts of the span may also be rotated with respect to each other around the longitudinal axis of the bridge. Even for a bridge with a span of approx. 2.8 μm length the span is still monocrystalline except for the central defect. The transition between span and pillars as well as the central defect look similar to the respective ones of the bridge shown in Fig. 2a. As this bridge is of identical height we can conclude that strain and defects are more strongly influenced by the height of the bridge than by its length.

V. MAGNON DYNAMICS

A major quality criterion for YIG structures is the Gilbert damping observed in ferromagnetic resonance (FMR). Two kinds of experiments are performed. The amount of material in a single bridge is very small and inductively detected FMR from a single bridge would thus result in a very small signal. We have performed FMR measurements on arrays of nominally identical bridges. The experiments were done using a waveguide which was deposited on a sample using electron beam lithography, metal evaporation and lift-off. Lithography was done after the annealing of the bridges and it is noteworthy that neither the spin-coating nor the lift-off harm the bridges in any way. The array under investigation contains 8000 bridges with an area of the free span between the pillars of 2700 x 600 nm. FMR measurements at 9.6 GHz show a linewidth of approx. 1 mT. The fact that this value is larger than for continuous films^{27,28} can easily be explained by taking into account that the measured

signal is the sum of the individual responses of 8000 different bridges. As will be shown below, the broadening is not due to material deterioration but caused by small differences in line position for the individual bridges. It is noteworthy that for 8000 bridges the line positions do not fluctuate by more than ± 0.5 mT. Also the Gilbert damping determined for the full array (see supplementary material) is $\alpha = (4.1 \pm 1.3) \times 10^{-4}$. In order to obtain a more detailed and accurate picture of the local spin dynamics further investigations are carried out by time-resolved scanning Kerr microscopy (TR-MOKE). Using this method we are able to image directly the different resonant magnon modes in individual bridges. The measurements are performed with the external magnetic field oriented along the bridge so backward volume modes (BVM) propagate along the bridge while Damon Eshbach modes (DEM) propagate at an angle of 90°. Fig. 3(top row) shows a number of different modes for increasing magnetic field. The ground mode with only one antinode is shown in Fig. 3b. Three standing BVM with nodes distributed along the bridge are shown in Fig. 3c-e, while a DEM mode shows a node extending along the bridge (Fig. 3a). It is clearly visible that the magnons are localized in the span of the bridge and no direct coupling to the feet or beyond is observed. Because of the complexity of the spectrum and the stability of the measurement it is difficult to obtain a frequency dependent line width in order to determine the damping. From our data we find a Gilbert damping value of the main resonance of $\alpha \approx (2.42 \pm 0.54) \times 10^{-4}$. We would like to emphasize that the absolute resonance line width is very small (approx. 140 μT at 8 GHz) indicating that the inhomogeneous linewidth at zero field ΔH_0 is very small (73.0 \pm 9.9) μT (see also Fig. 5 supplementary material).

We have also modelled the different magnon modes using MuMax3³⁰. Fig. 3(bottom row) shows the respective simulations, which are in good agreement with our experiments. It should be noted that the fabrication process is not limited to single bridges but is highly flexible and can be extended to more complex structures as shown in Fig. 4.

VI. CONCLUSION

It is possible to fabricate 3D YIG nanobridges by molding the material using electron beam lithography, room temperature PLD and lift-off. Crystallization during the annealing process progresses throughout the bridge on a length scale of more than one μm leading to an undisturbed lattice with only few defects. The span of the bridge typically contains a single defect. The damping does not reach the record values of low temperature grown layers but is still in the range of high quality PLD grown YIG films. The minimum line width of 140 μT for a single bridge is well in the range of high quality thin film material and various resonant magnon modes can be identified in TR-MOKE. As a next step more

complex resonators are fabricated and investigated which then need to be optimized not only for magnons but also for the coupling to mechanical oscillations. Based on this class of nano-resonators new schemes may be developed to transfer information from qubits to mechanical oscillations via magnons. The new technology can allow these schemes to be realized on the micron scale or below, making future integration a real option.

VII. METHODS

A. Electron beam lithography

The feet and the span of the bridge are exposed using two different acceleration voltages, respectively. The span is exposed at 2.8 kV while the acceleration voltage for the feet is 4.5 kV. For both exposures the area dose is $100 \mu\text{C}/\text{cm}^2$. The structures are developed for 60 s in isopropanol.

B. YIG deposition

The YIG is deposited in 0.025 mbar of oxygen from a home-made target. Laser parameters are 248 nm wavelength, fluency of 2.5 J cm^{-2} , and a frequency of 5 Hz. Annealing is done in a pure oxygen atmosphere (99.997%) at ambient pressure at 800°C for 3 hours.

C. TEM preparation

TEM samples from bridges are prepared using a focused gallium ion beam FEI VERSA 3D dual beam microscope by the classical FIB in-situ lift-out technique as described for instance in³¹. Due to the electrically isolating substrate this procedure is extended for the preparation of the sample after thermal treatment by depositing a thin conductive carbon layer via ion sputtering before transferring the sample to the FIB. As the first step in the preparation procedure inside the FIB a 200 nm thick carbon layer is deposited locally using the electron beam

at 5 kV from the top through the bridge to fill the space under the bridge with carbon. The hole under the bridge is filled by locally cracking the organometallic complex gas from the platinum Gas Injection System of the FIB with a 5 kV electron beam. After lift-out the TEM lamellae are mounted to a grid, thinned down to a thickness below 150 nm, and stepwise cleaned on both sides from amorphous material by operating the ion beam of the FIB at 5 kV, 2 kV and 1 kV. HRTEM images from these samples are obtained using a JEOL JEM-4010 TEM operated at 400 kV.

D. Time resolved MOKE

For the time resolved magneto optic Kerr (TR-MOKE) measurements we use a frequency doubled fs-laser operating at 520 nm to illuminate the sample in a scanning optical microscope with polarization analysis. A detailed description of this method is presented in³². In our TR-MOKE measurements the magnetization is excited by continuous wave microwave magnetic field which is phase synchronized to the optical probe pulses, i.e. the sampling is stroboscopic. In order to allow for lock-in amplification of the magneto-optical signal the rf-excitation is modulated^{33,34}. The spatial resolution of the measurements presented in this manuscript is diffraction-limited to about 300 nm.

E. Micromagnetic simulation

The simulations were carried out using MuMax3. The simulated structure is a bridge with a rectangular span of $2700 \text{ nm} \times 600 \text{ nm} \times 110 \text{ nm}$ (l x w x h). The feet are $300 \text{ nm} \times 600 \text{ nm} \times 110 \text{ nm}$. After relaxing the structure in the external magnetic field H_0 in x-direction a small field step perpendicular to the surface (z) is applied. The following precession in the z/y-plane is recorded and a FFT is performed. In the FFT the main oscillations are identified as peaks in the amplitude. The images are obtained by locally evaluating the amplitude and phase of the precession and transforming them into a color (intensity = amplitude, positive phase: red, negative phase: blue).

* Correspondence to G. Schmidt: georg.schmidt@physik.uni-halle.de

¹ M. D. LaHaye, J. Suh, P. M. Echternach, K. C. Schwab, and M. L. Roukes, *Nature* **459**, 960 (2009).

² A. P. Reed, K. H. Mayer, J. D. Teufel, L. D. Burkhardt, W. Pfaff, M. Reagor, L. Sletten, X. Ma, R. J. Schoelkopf, E. Knill, et al., *Nature Physics* **13**, 1163 (2017).

³ R. W. Andrews, A. P. Reed, K. Cicak, J. D. Teufel, and K. W. Lehnert, *Nature Communications* **6**, 10021 (2015), 1506.02296.

⁴ F. Lecocq, J. B. Clark, R. W. Simmonds, J. Aumentado, and J. D. Teufel, *Physical Review Letters* **116**, 043601

(2016), 1512.00078.

⁵ C. F. Ockeloen-Korppi, E. Damskäg, J.-M. Pirkkalainen, T. T. Heikkilä, F. Massel, and M. A. Sillanpää, *Physical Review X* **6**, 041024 (2016), 1602.05779.

⁶ T. Kasuya and R. C. Lecraw, *Physical Review Letters* **6**, 223 (1961).

⁷ E. Schlömann, *Journal of Applied Physics* **31**, 1647 (1960).

⁸ X. Zhang, C.-L. Zou, L. Jiang, and H. X. Tang, *Science Advances* **2**, e1501286 (2016), 1511.03680.

⁹ A. V. Chumak and H. Schultheiss, *Journal of Physics D Applied Physics* **50**, 300201 (2017).

¹⁰ M. B. Jungfleisch, W. Zhang, W. Jiang, H. Chang, J. Skle-

- nar, S. M. Wu, J. E. Pearson, A. Bhattacharya, J. B. Ketterson, M. Wu, et al., *Journal of Applied Physics* **117**, 17D128 (2015), 1412.4032.
- ¹¹ S. Li, W. Zhang, J. Ding, J. E. Pearson, V. Novosad, and A. Hoffmann, *Nanoscale* **8**, 388 (2015), 1512.00286.
- ¹² M. Collet, X. de Milly, O. D'Allivy Kelly, V. V. Naletov, R. Bernard, P. Bortolotti, J. Ben Youssef, V. E. Demidov, S. O. Demokritov, J. L. Prieto, et al., *Nature Communications* **7**, 10377 (2016), 1504.01512.
- ¹³ N. Zhu, H. Chang, A. Franson, T. Liu, X. Zhang, E. Johnston-Halperin, M. Wu, and H. X. Tang, *Applied Physics Letters* **110**, 252401 (2017), 1704.03056.
- ¹⁴ M. Collet, O. Gladii, M. Evelt, V. Bessonov, L. Soumah, P. Bortolotti, S. O. Demokritov, Y. Henry, V. Cros, M. Bailleul, et al., *Applied Physics Letters* **110**, 092408 (2017), 1610.08756.
- ¹⁵ K. Vogt, F. Y. Fradin, J. E. Pearson, T. Sebastian, S. D. Bader, B. Hillebrands, A. Hoffmann, and H. Schultheiss, *Nature Communications* **5**, 3727 (2014).
- ¹⁶ A. V. Chumak, A. A. Serga, and B. Hillebrands, *Nature Communications* **5**, 4700 (2014).
- ¹⁷ T. Fischer, M. Kewenig, D. A. Bozhko, A. A. Serga, I. I. Syvorotka, F. Ciubotaru, C. Adelman, B. Hillebrands, and A. V. Chumak, *Applied Physics Letters* **110**, 152401 (2017), 1612.07708.
- ¹⁸ A. V. Sadovnikov, S. A. Odintsov, E. N. Beginin, S. E. Sheshukova, Y. P. Sharaevskii, and S. A. Nikitov, *Physical Review B* **96**, 144428 (2017).
- ¹⁹ Y. Tabuchi, S. Ishino, A. Noguchi, T. Ishikawa, R. Yamazaki, K. Usami, and Y. Nakamura, *Science* **349**, 405 (2015), 1410.3781.
- ²⁰ Y. Chu, P. Kharel, W. H. Renninger, L. D. Burkhardt, L. Frunzio, P. T. Rakich, and R. J. Schoelkopf, *Science* **358**, 199 (2017), 1703.00342.
- ²¹ A. D. O'Connell, M. Hofheinz, M. Ansmann, R. C. Bialczak, M. Lenander, E. Lucero, M. Neeley, D. Sank, H. Wang, M. Weides, et al., *Nature* **464**, 697 (2010).
- ²² X. M. Henry Huang, C. A. Zorman, M. Mehregany, and M. L. Roukes, *Nature* **421**, 496 (2003).
- ²³ A. Yacoby, M. Heiblum, D. Mahalu, and H. Shtrikman, *Physical Review Letters* **74**, 4047 (1995).
- ²⁴ M. E. Sherwin, J. A. Simmons, T. E. Eiles, N. E. Harff, and J. F. Klem, *Applied Physics Letters* **65**, 2326 (1994).
- ²⁵ T. Borzenko, C. Gould, G. Schmidt, and L. Molenkamp, *Microelectronic Engineering* **75**, 210 (2004).
- ²⁶ M. P. Schwarz, D. Grundler, I. Meinel, C. Heyn, and D. Heitmann, *Applied Physics Letters* **76**, 3564 (2000).
- ²⁷ C. Hauser, T. Richter, N. Homonnay, C. Eisenschmidt, M. Qaid, H. Deniz, D. Hesse, M. Sawicki, S. G. Ebbinghaus, and G. Schmidt, *Scientific Reports* **6**, 20827 (2016).
- ²⁸ C. Hauser, C. Eisenschmidt, T. Richter, A. Müller, H. Deniz, and G. Schmidt, *Journal of Applied Physics* **122**, 083908 (2017).
- ²⁹ H. Chang, P. Li, W. Zhang, T. Liu, A. Hoffmann, L. Deng, and M. Wu, *IEEE Magnetics Letters* **5**, 6700104 (2014).
- ³⁰ A. Vansteenkiste, J. Leliaert, M. Dvornik, M. Helsen, F. Garcia-Sanchez, and B. Van Waeyenberge, *AIP Advances* **4**, 107133 (2014), 1406.7635.
- ³¹ S. Bals, W. Tirry, R. Geurts, Z. Yang, and D. Schryvers, *Microscopy and Microanalysis* **13**, 80 (2007).
- ³² M. Farle, T. Silva, and G. Woltersdorf, *Spin Dynamics in the Time and Frequency Domain* (Springer Berlin Heidelberg, Berlin, Heidelberg, 2013), pp. 37–83, ISBN 978-3-642-32042-2.
- ³³ G. Woltersdorf, O. Mosendz, B. Heinrich, and C. H. Back, *Physical Review Letters* **99**, 246603 (2007).
- ³⁴ J. Stigloher, M. Decker, H. S. Körner, K. Tanabe, T. Moriyama, T. Taniguchi, H. Hata, M. Madami, G. Gubbiotti, K. Kobayashi, et al., *Physical Review Letters* **117**, 037204 (2016), 1606.02895.

F. Acknowledgements

This work was supported by the DFG in the SFB 762. We thank the Max-Planck-Institut für Mikrostrukturphysik for the making the JEOL JEM-4010 TEM available for our experiments.

G. Competing Interests

The authors declare that they have no competing financial interests.

H. Author contributions

F.H. developed the process and performed transmission electron microscopy and analysis, C. Hauser performed inductive FMR and PLD, P.T. performed electron beam lithography and PLD and improved the process, P.G. performed the micromagnetic simulations, F.S. performed SEM imaging, R.D. performed TR-MOKE and analysis, S.G.E. prepared the PLD targets, G.W. planned the TR-MOKE experiments and contributed to the manuscript, G.S. planned the process and the characterization, supervised the experiments and wrote the manuscript).

I. Correspondence

Correspondence and requests for materials should be addressed to Georg Schmidt (email: georg.schmidt@physik.uni-halle.de).

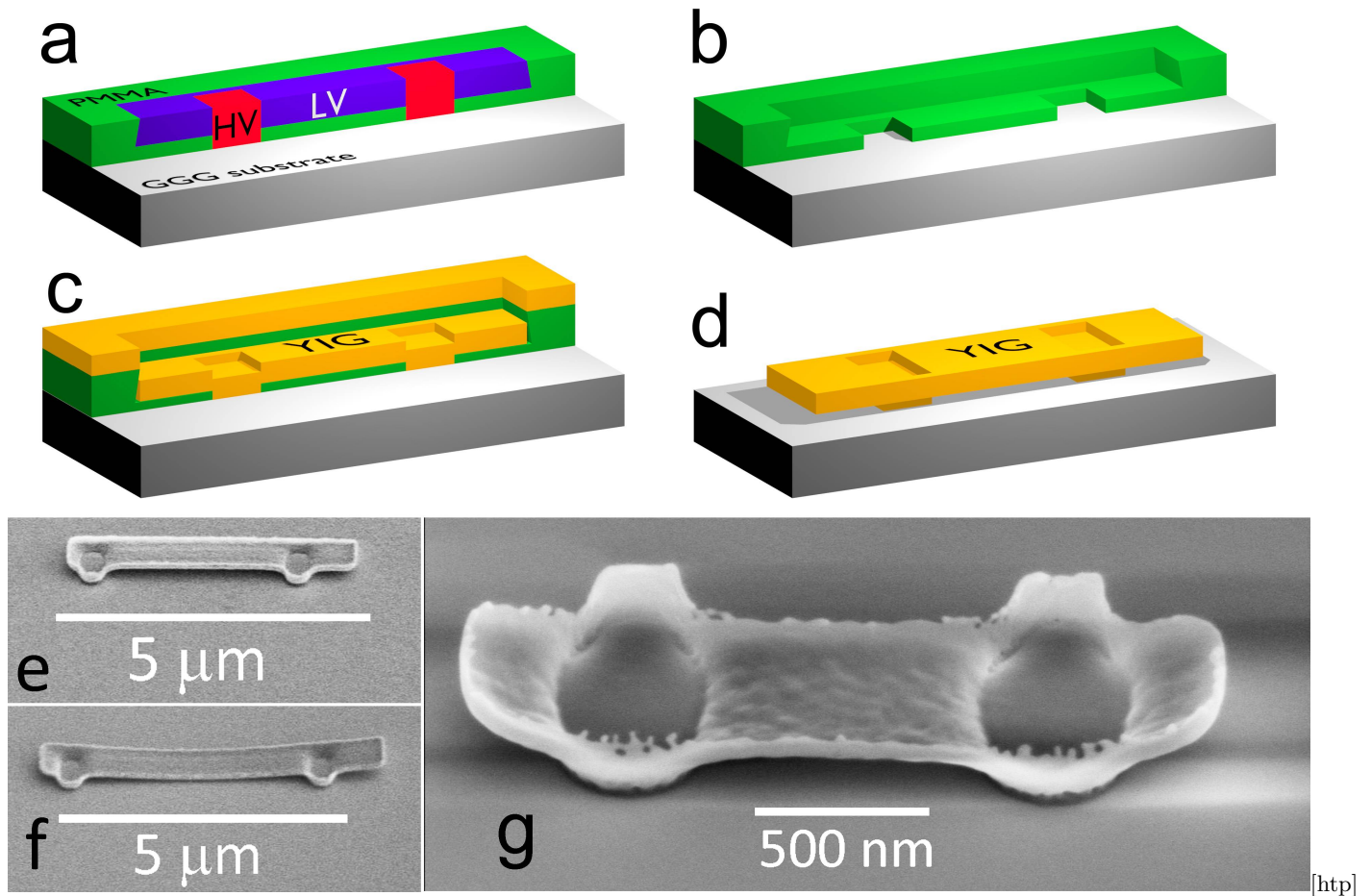


FIG. 1: Schematic drawing of the process flow for patterning and results. (a) A resist (green) is exposed with two different acceleration voltages. A low voltage exposure is used for the span of the bridge (blue) and a high acceleration voltage (red) exposes the pillars down to the substrate. (b) After development the void in the resist has the shape of the bridge and a slight undercut which later facilitates the lift-off. (c) The YIG is deposited and the shape of the bridge becomes visible. It is important that the YIG on the resist surface is well separated from the bridge itself. (d) After lift-off a free-standing bridge is obtained. (e-f) SEM images of different bridges before (e) and after annealing (f).

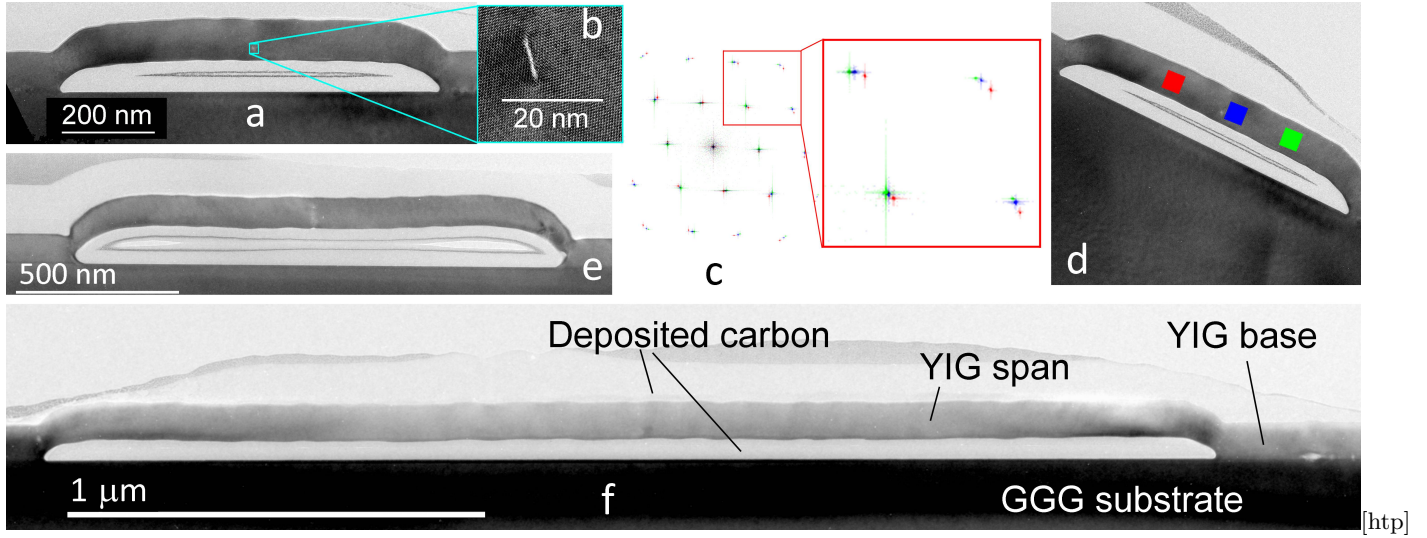


FIG. 2: Results from transmission electron microscopy. (a) A bridge with a span of approx. 850 nm length and a height of 75 nm underneath the span. (b) Further magnification shows a single defect in the center of the bridge. (c) Superposition of Fourier transforms in three different colors from three different respective places (d) in one bridge. The superposition shows that the lattice in each place is slightly rotated with respect to the others. (e) TEM cross section of a bridge with increased height or (f) increased length. Even for a length of 2800 nm the bridge is defect free except for the central defect. Above and below the bridge a carbon film is visible which has been deposited using the electron beam during TEM preparation to protect the surface of the bridge.

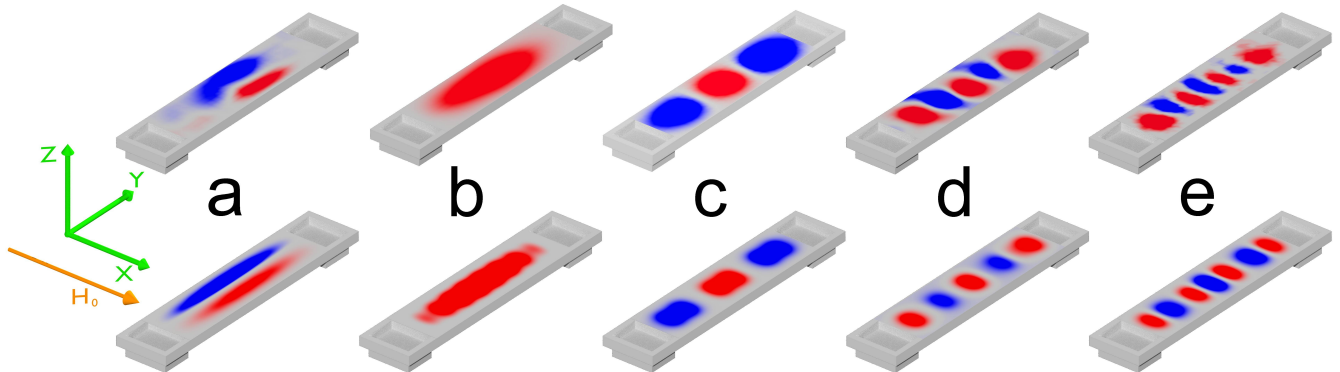


FIG. 3: Time-resolved scanning Kerr microscopy (TR-MOKE) images of standing spin-wave modes and simulations. The top row shows TR-MOKE results for the main mode (b), one Damon Eshbach mode (a), and three different backward volume modes (c-e). Measurement parameters are (magnetic field@frequency) 11.96 mT@2 GHz (a), 21.95 mT@2 GHz (b), 25.61 mT@2 GHz (c), 89.72 mT@4 GHz (d), and 92.52 mT@4 GHz (e). The measurements were done by varying the magnetic field at fixed frequency. The bottom row shows the corresponding simulation results from simulations at fixed respective magnetic fields (see also methods section). Simulation parameters are 19.4 mT@2.32 GHz (a), 19.4 mT@2.00 GHz (b), 19.4 mT@1.85 GHz (c), 83.8 mT@3.73 GHz (d), and 83.8 mT@3.66 GHz (e). The coordinate system on the left hand side shows the orientation of the external magnetic field H_0 .

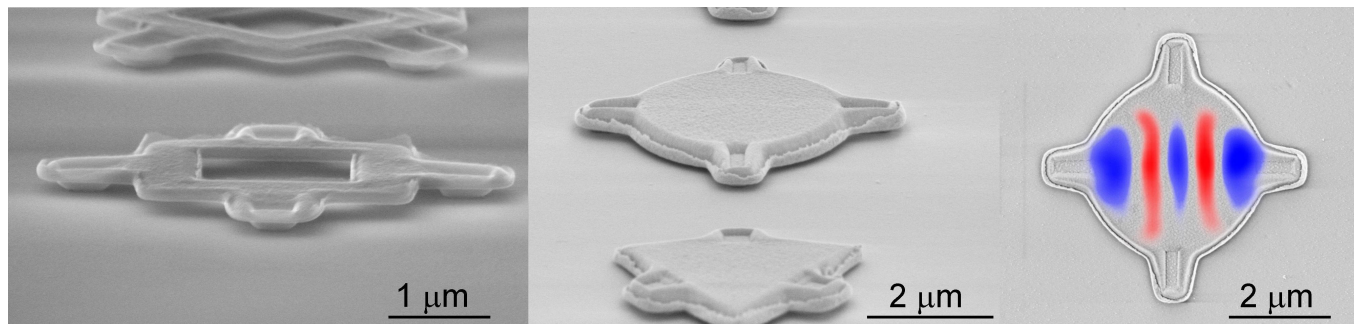


FIG. 4: SEM images of more complex resonators. The process allows to fabricate various shapes such as open squares (a) or disks and triangles (b). (c) TR-MOKE image of a standing BVM measured on a disk resonator overlaid to an SEM image of a similar structure.

Supplementary material to: Monocrystalline free standing 3D yttrium iron garnet magnon nano resonators

I. FERROMAGNETIC RESONANCE

Ferromagnetic resonance spectra have been taken by two different methods. Inductive measurements are performed on an array of 8000 nominally identical bridges with a respective span of $2700 \times 600 \text{ nm}^2$. The array is placed in the gap of a coplanar waveguide (CPW) deposited on the sample by electron beam lithography, metallization and lift-off. The CPW is used to apply the RF magnetic field for excitation, which in this geometry is out-of-plane. At fixed RF-frequencies the external magnetic field is varied and a spectrum is acquired. Increased sensitivity is achieved by modulating the external magnetic field and using lock-in detection resulting in a measurement of the absorptions derivative. The procedure is repeated at different frequencies. By extracting the line width at different frequencies it is possible to determine the Gilbert damping. In the following this method will simply be referred to as FMR. A similar procedure is used and combined with time resolved scanning Kerr microscopy (TR-MOKE) on the same sample. In the TR-MOKE experiment the precession is not measured inductively from the array but determined from the Kerr effect generated in an individual bridge onto which the light is focussed into a diffraction limited spot of 300 nm. Two spectra obtained by these respective methods, are shown in Fig. 1. The FMR signal has been integrated for better comparability. The spectra look considerably different. Especially the line width for the inductive measurement ($\Delta H < 1.25 \text{ mT}$) is almost a factor of 10 larger than for the spectrum obtained by TR-MOKE ($\Delta H < 0.14 \text{ mT}$).

In order to understand this difference we have to take several things into account. The TR-MOKE spectrum is taken on a fixed point of the span of a single bridge. It clearly shows two separate modes very close to each other which even partly overlap. If on a different position on the span the resonance frequency is slightly shifted (for example because of variations of the local field) the two lines may become undistinguishable and appear as a broader line. This effect, however, is expected to be much smaller than the line broadening in the inductive measurement. Another cause of broadening is the variation of the resonance field between the individual bridges. Fig. 2 shows TR-MOKE images of five different bridges obtained simultaneously and repeated for two different magnetic fields. For individual bridges the main resonance (only one antinode) appears at fields that vary by almost 0.8 mT, respectively.

As the inductive measurement only shows the integrated signal of 8000 bridges obtained by FMR. In this case the individual bridge resonance is convoluted with a distribution function of the resonance fields in the array. Finally a third effect can be identified in Fig. 3. Although the span of the bridge yields the main signal the feet and the overhang at the end of the bridge also show a localized resonance mode. The overhang has similar properties as the span. Fig. 3 indeed shows that the overhang has its main resonance at a field offset by approx. 7 mT from the main resonance field of the corresponding span.

This is more than the line broadening observed in the inductive experiment. It should be noted, however, that in the inductive experiment additional modes are observed, one of them with a smaller amplitude and approx. 7 mT below the main resonance. This indicates that the line broadening is mainly caused by the overlap of narrow lines because of inhomogeneous resonance fields along the bridge and variations of the resonance fields between bridges. It is noteworthy that even for 8000 bridges the distribution of resonance fields amounts to only 1 mT. Resonances within different parts of the bridge (overhang vs. span), however, lead to the appearance of well resolved additional features.

II. GILBERT DAMPING

In a next step the resonance frequencies were plotted over the respective magnetic field (Fig. 4) and the data was fitted by the Kittel formula:

$$\omega = \mu_0 \gamma \sqrt{H_{FMR}(H_{FMR} + M_{eff})} \quad (1)$$

to obtain the effective saturation magnetization M_{eff} which also contains any anisotropy and the gyromagnetic ratio γ . For the FMR measurements this yields $\gamma = (171.8 \pm 2) \text{ GHz/T}$ and $M_{eff} = (0.145 \pm 0.007) \text{ T}$.

For the TR-MOKE the values are $\gamma = (180.3 \pm 0.6) \text{ GHz/T}$ and $M_{eff} = (0.125 \pm 0.003) \text{ T}$. The deviation between the methods is most likely due to the line broadening in the FMR discussed above. Due to this broadening the line position in FMR may be more difficult to determine and will also show an average value, while the resonance field of the single bridge in TR-MOKE can deviate from the average value. To determine the Gilbert damping a plot of line width as a function of frequency is used (Fig. 5). For the FMR the broadening and the presence of multiple lines

only allows for the extraction of the line width at frequencies of 8 GHz and above. Here the fitted data yields a Gilbert damping of $\alpha \approx (4.1 \pm 1.3) \times 10^{-4}$. For TR-MOKE a more reliable analysis is possible, since the data can be fitted to Lorentzian line shapes. The resulting value of the damping is $\alpha \approx (2.42 \pm 0.54) \times 10^{-4}$. The latter is close to the best values obtained for thin film YIG. Also the intrinsic line width for zero field is very low with a value of only $(73.0 \pm 9.9) \mu\text{T}$.

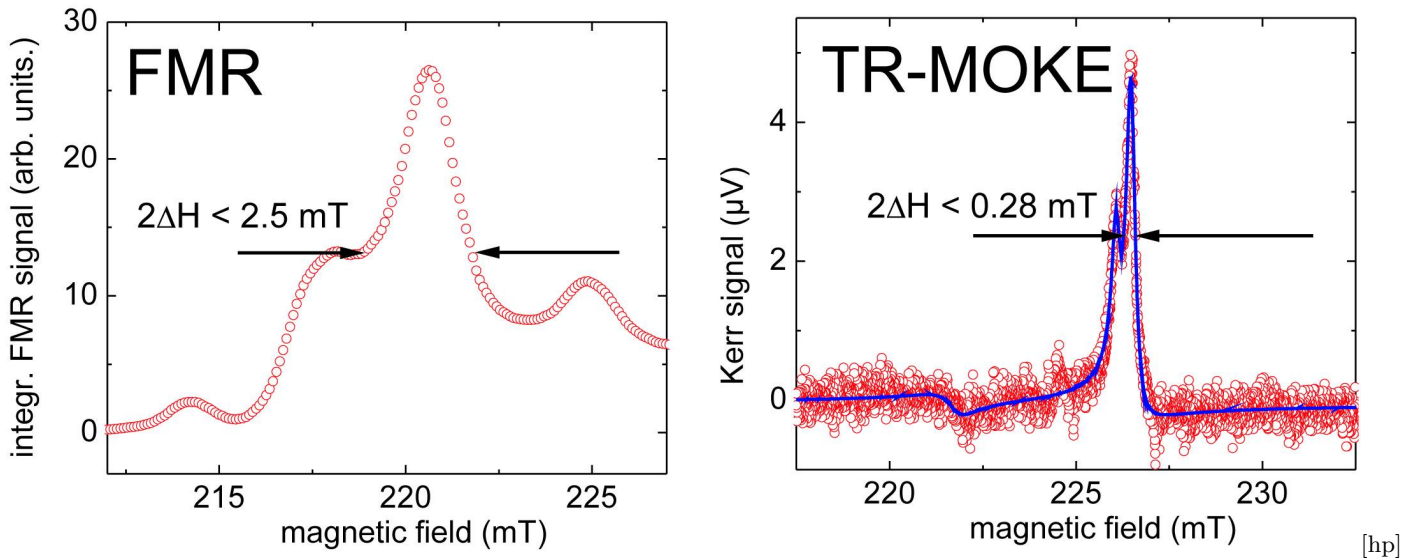


FIG. 1: FMR spectra obtained by inductive measurements on an array of 8000 nominally identical bridges and by TR-MOKE on a single bridge. The red circles show the measured data while the blue line is a fit using three Lorentzian line shapes. The arrows are a guide to the eye showing an upper limit for the full width at half maximum which is $2\Delta H$. The half width at half maximum ΔH is mostly referred to in literature as the line width. The TR-MOKE measurement which is performed on a single spot with a diameter of approx. 300 nm shows only two very sharp lines with a small overlap. The line width ΔH is smaller than $140 \mu\text{T}$. The FMR measurement, however, shows a much broader line ($\Delta H < 1.25 \text{ mT}$), and additional modes because the signal is integrated over 8000 individual bridges including the span and the overhang.

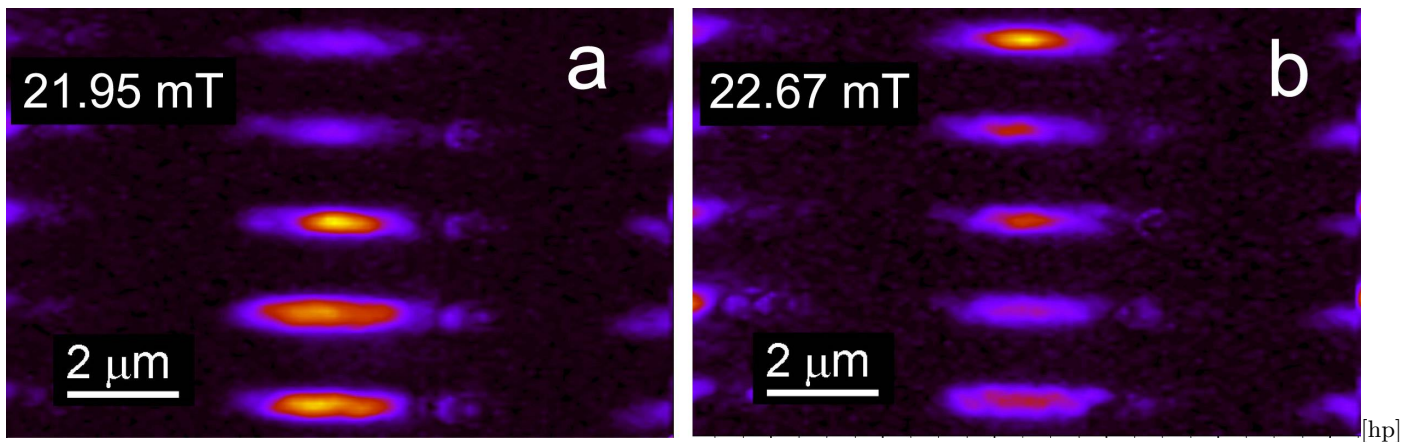


FIG. 2: Two TR-MOKE images obtained at a frequency of 2 GHz showing five adjacent bridges at two different magnetic fields, respectively. In both images at least one of the bridges shows an intense resonance of the mode with one antinode only. Apparently the resonance field between bridges can vary at least by 0.8 mT.

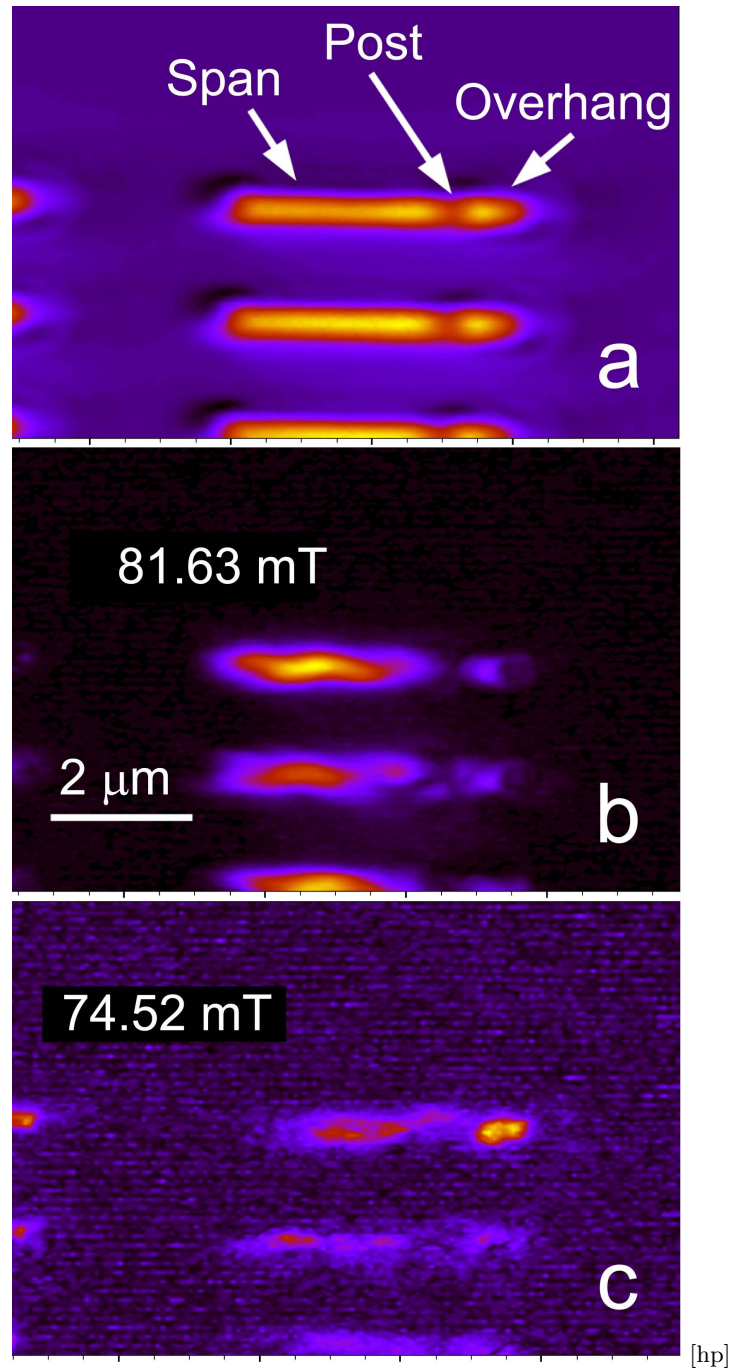


FIG. 3: Optical topography image of several bridges (a) and two TR-MOKE images of the same area acquired at a frequency of 6 GHz at different respective magnetic fields (b-c). In the topography image we can clearly discern the span of the bridge, the base which is slightly darker and the overhang at the end. (b) Shows the main resonance of the span with one antinode while in (c) a similar mode for the overhang of the same bridge is observed. The resonance fields differ by 7 mT.

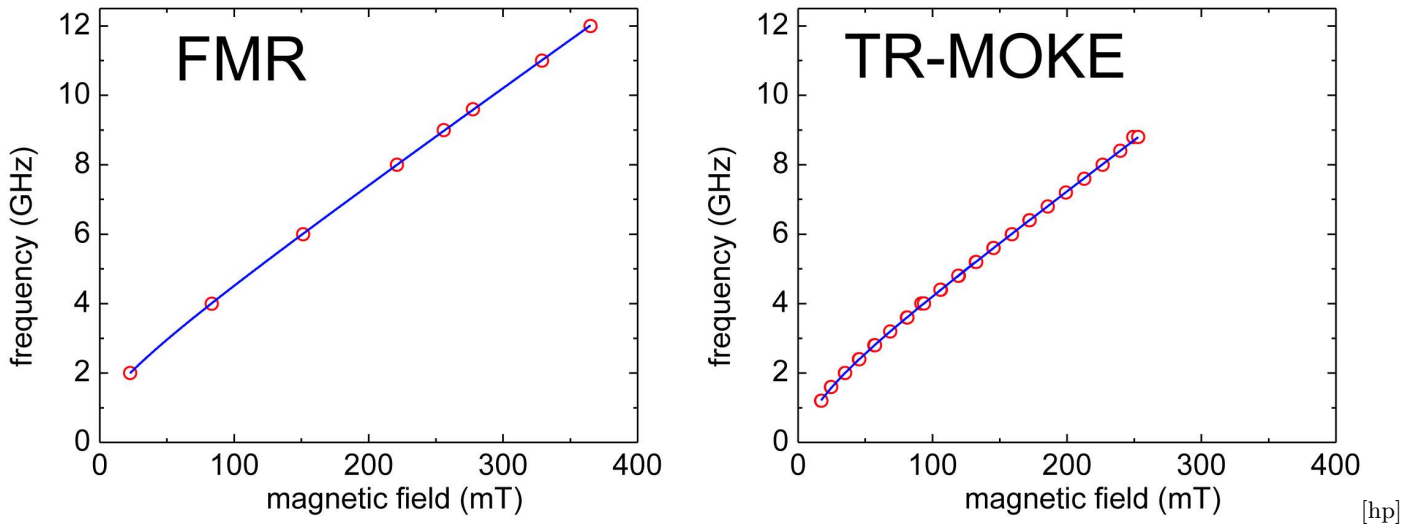


FIG. 4: Resonance frequency plotted as a function applied magnetic field for FMR (left) and TR-MOKE (right) measurements. The results nicely agree except for small deviations at low magnetic fields. The red circles show the measured data while the blue line is the respective fit using the Kittel formula.

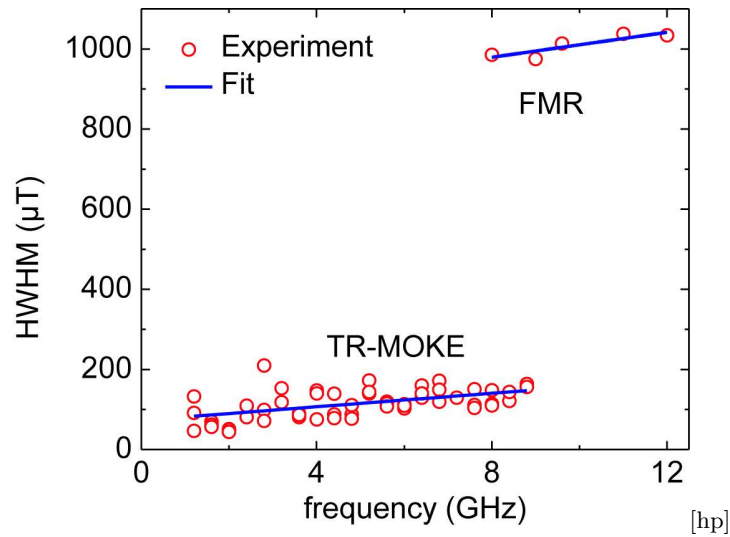


FIG. 5: HWHM ΔH plotted as a function the resonance frequency. For the FMR the linewidth could only be extracted at frequencies above 8 GHz. The circles show the measured data while the lines show the respective fit according to which the Gilbert damping is determined.